Optics Communications 493 (2021) 126994

Contents lists available at ScienceDirect

Optics Communications

journal homepage: www.elsevier.com/locate/optcom

Gate-controlled graphene surface plasmon resonance glucose sensor

Md. Mahbub Hossain, Muhammad Anisuzzaman Talukder *

Department of Electrical and Electronic Engineering, Bangladesh University of Engineering and Technology, Dhaka 1205, Bangladesh

ARTICLE INFO

Keywords:
Graphene
Surface plasmon resonance
SPR sensors
Graphene sensors

ABSTRACT

We propose a surface plasmon resonance (SPR) glucose sensor where a graphene mono-layer is used with controllable optical property by applying a gate voltage. We show that the gate voltage to the graphene mono-layer can increase the light absorption, and hence, the sensitivity of the proposed glucose sensor significantly. We find that the sensitivity and figure-of-merit of the proposed sensor increase by 21.48% and 49.57% when a 20-V gate voltage is applied to the graphene mono-layer compared to that when there is no gate voltage applied to the graphene mono-layer. We present a linear regression analysis for measuring the blood sugar level (BSL) using the proposed sensor that shows a highly reliable performance of the proposed sensor. We also present the effects of temperature on the proposed sensor performances. We find that the error in the detection of BSL remains within 4.75% on average and within 7.40% in the worst-case scenario when temperature varies by ±10 °C from a reference 25 °C. Comparisons of the proposed sensor with several state-of-the-art sensors show a significantly enhanced behavior, as well as the error induced due to the change in temperature is much smaller than that of 15%, which is used as an allowable error limit for off-the-shelf glucose meters.

1. Introduction

Diabetes is a common disease that affected approximately 463 million people in 2019 and may affect 700 million by 2045 [1]. Unrestrained diabetes creates many health problems, including damage to blood vessels and nerves, loss of kidney function and vision, stroke, heart attack, lower limb seizures, brain dysfunction, and early mortality [2]. Diabetes is a threat all over the world and a leading health problem for low- and middle-income countries [3]. The treatment of diabetes patients crucially depends on the fast and accurate measurement of the blood sugar level (BSL), especially when patients suffer from deficient BSL, i.e., in hypo and hyperglycemia conditions.

Usually, the BSL detection devices—commonly known as glucometers—use reflection photometry or electrochemical techniques [4]. Although the photometry technique offers high precision, its use in glucometers is limited due to the time-consuming sample preparation, requirement of regular calibration, and optical interference that affects results. By contrast, an electrochemical technique, although not as precise as photometry technique [5], is usually preferred for offering high sensitivity (S), low-cost, easy maintenance, and good reproducibility. Current off-the-shelf glucometers commonly use test strips containing glucose oxidase (GO) enzyme that reacts to blood sugar. When an electrical potential is applied across the strip, an electrical current is generated with a magnitude that depends on the BSL. In practice, glucometers must have a readout deviation of $\leq$ 15% from the actual BSL at 95% times, according to regulatory authorities [6]. Crucially, ~15% deviation of the test results with electrochemical glucometers could be detrimental, especially when a person is on the borderline in the blood sugar map or critically ill who needs immediate and appropriate medication. Additionally, the chemical enzyme used in the test strips of electrochemical glucometers is sensitive to environmental factors such as the temperature and humidity. The test strips that are exposed to dry and hot weather during packaging and shipping may have altered chemistry and reactivity of enzymes so much to affect the test results significantly [7].

Optical biosensors have shown promises in applications related to food security, biological substances monitoring, biomedical research, and disease detection [8–12]. However, the work on optical biosensors for glucose detection is still scarce. The detection of glucose or BSL using a spectral analysis of the reflected light profile and glucose-1-dehydrogenase, hexokinase, and GO enzymes based immobilization has been demonstrated [13,14]. However, these optical biosensors require long detection time. Recently, diverse optical sensing techniques using photonic crystal fibers (PCFs), interferometers, resonant cavities, and mid-infrared photo-acoustics have been proposed to detect the BSL [15]. In particular, PCF-based glucose sensors offer high design flexibility and sensitivity, and large refractive index variation [15,16]. Nevertheless, PCF-based sensors are not suitable for everyday glucometers for their intricate fabrication complexity [17].

During the last few decades, optical biosensors based on surface plasmon resonance (SPR) have attracted a significant interest for diagnosis of diseases. SPR biosensors do not require labels to detect the

* Corresponding author.
E-mail address: anis@eee.buet.ac.bd (M.A. Talukder).

https://doi.org/10.1016/j.optcom.2021.126994
Received 20 November 2020; Received in revised form 14 March 2021; Accepted 31 March 2021
Available online 6 April 2021

sample. Additionally, SPR biosensors offer advantages over other label-free biosensing techniques in real-time monitoring of bio-molecule interactions, affinity, specificity, and kinetics during the bindings of bio-molecules [18–20]. SPR sensors such as gold (Au)-coated dielectric materials have been proposed for the detection of glucose in blood, offering high accuracy and resolution [21]. However, such Au-coated SPR sensors suffer from chemical noise in the measurement and poor absorption of the incident light. Recently, an Au-chromium (Cr) nano-laminated SPR sensor has shown good performance in glucose detection [22], although it suffers from a limited detection range of the BSL.

To increase the sensitivity of SPR-based sensors, several research groups have proposed the use of graphene layers [18,23–28]. In practice, the excitation of surface plasmon polaritons (SPPs) in graphene is difficult due to the momentum mismatch between the incident light and graphene plasmons. To date, several schemes have been exploited to excite SPPs in graphene, including employing prism coupling [29], sub-wavelength silicon grating [30], and resonant optical antennas [31]. A graphene mono-layer has zero band gap in the visible wavelength range and absorbs only ∼2.3% of the incident light [32]. Therefore, multiple graphene layers and transition-metal-dichalcogenides (TMDC) or nano-structures on graphene layers are often used to increase the sensitivity and figure-of-merit (FoM) of biosensors [18,33–35]. However, the increase of graphene layers broadens the full-width at half-maximum (FWHM) of the absorption profile, and the use of TMDC or nano-structures makes biosensor structures complex and costly [33].

In this work, we propose a gate-controlled graphene SPR glucose sensor. We modify the mono-layer graphene Fermi energy (E_f) by a gate voltage (V_g) to increase the absorption, and hence, improve the sensitivity and FoM of the proposed sensor. The proposed sensor does not require labels or an extensive sample preparation. The proposed sensor is highly sensitive and selective to BSL, and less sensitive to environmental variations when compared to the state-of-the-art glucose sensors.

To determine the sensor performance parameters, we use a transfer matrix method (TMM) based angular interrogation technique. We calculate mono-layer graphene conductivity using the Kubo formula for different applied V_g at 633 nm incident wavelength. To determine the measurement accuracy of BSL, we use a linear regression model. Our proposed gate-controlled graphene SPR glucose sensor offers significant improvement in the detection sensitivity and FoM compared to that of state-of-the-art SPR biosensors. Furthermore, our proposed glucose sensor shows a detection error $\ll$ 15% that is used as a tolerable performance for state-of-the-art glucose meters.

The rest of the paper is organized as follows: In Section 2, we present the proposed sensor configuration. In Section 3, we describe the theoretical models that we used to calculate the graphene optical properties and the sensor performance when V_g is applied. We discuss the simulation approaches that we followed to solve the Maxwell equations using finite difference time domain (FDTD) technique in Section 4. We present and discuss the calculated sensor performances and measurement accuracy of BSL for different V_g in Section 5. Additionally, in Section 5, we analyze the effect of temperature on the detection of BSL. In Section 6, we draw conclusions on the findings.

2. Sensor configuration

The proposed gate-controlled graphene SPR glucose sensor consists of eight layers, as shown in Fig. 1. The first layer is a semi-infinite prism made of borosilicate (BK7) glass material. The light is incident on the multi-layer sensor structure through the prism, and the reflected light intensity is recorded from the prism as well. A silver (Ag) layer follows the prism with an air gap between them. The air gap helps to increase the resonance dip of the reflection (R) profile [36]. The thicknesses of the air gap and Ag are chosen following the analysis presented in Fig. 2. Fig. 2(a) shows the R profile of the proposed sensor as a function of

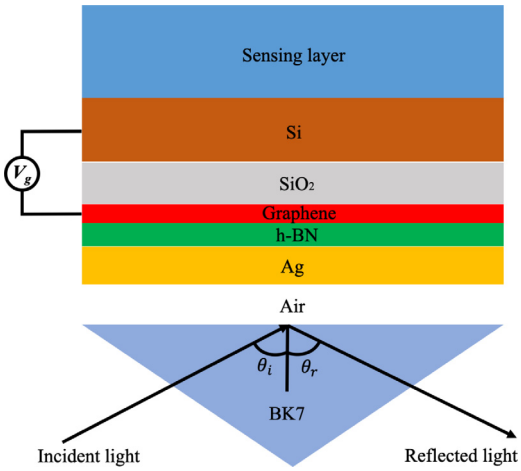

Fig. 1. Schematic illustration of the proposed gate-controlled graphene SPR glucose sensor.

the incidence angle (θ) of light for different thicknesses (d_{air}) of the air gap. The minimum value of R decreases as d_{air} decreases. In this work, d_{air} = 40 nm is chosen as an even smaller air gap will complicate the fabrication of the plano-convex singlet lens to create the air gap [37]. Fig. 2(b) shows R against θ for different thicknesses (d_{Ag}) of Ag. We note that the minimum R occurs at d_{Ag} = 45 nm. Therefore, d_{Ag} was chosen as 45 nm in this work.

An ultra-thin hexagonal boron nitride (h-BN) layer separates graphene from Ag. The h-BN layer has a thickness of 1 nm, which maximizes light absorption by the sensor [38]. The presence of h-BN between graphene and Ag increases the lifetime of the excited SPPs in the graphene layer [39,40]. The used graphene is mono-layer, i.e., the thickness is 0.34 nm. An increase in the number of graphene layer widens the R profile. In the visible and near-infrared frequencies, the permittivity (ε) of graphene mono-layer is controllable by an applied V_g. Thin layers of silicon dioxide (SiO_2) and silicon (Si) are added on the top of graphene for stronger absorption of the incident light [41]. Fig. 2(c) shows that R decreases as the SiO_2 thickness (d_{SiO_2}) decreases. In this work, d_{SiO_2} = 8 nm is chosen since the SiO_2 layer works as an insulating layer between the graphene and Si layer. The gate voltage V_g is applied between the graphene and Si layer to control the electron density (n) and E_f of graphene [41,42]. The thickness of Si layer is chosen as 50 nm to achieve high electric field [43]. The sensing medium, i.e., blood sample, is placed on the Si layer. In this work, a fixed 100-nm-thick sensing layer is assumed.

Practically, a thermal vapor deposition technique can be used to deposit Ag on the top of BK7 substrate [27]. The graphene layer can be deposited on h-BN by dissolving atomic carbon in vacuum using high temperature [27]. Different dielectric materials can be grown on top of each other using evaporation techniques [44].

3. Theoretical modeling

3.1. Optical properties

The response of the proposed sensor to an incident light will depend on the complex refractive indices of the materials in different layers. The response of the sensor will also depend on the wavelength of the incident light when a material has dispersive optical property. In this work, we investigate the sensor performance for an incident wavelength of 633 nm, which is often used in experiments for SPR-based techniques [45]. We follow an approach described in Ref. [23] to calculate the wavelength-dependent refractive index of BK7 prism. The refractive index of Ag is calculated using the Drude–Lorentz model [46], while the refractive indices of h-BN, SiO_2, and Si are obtained from the

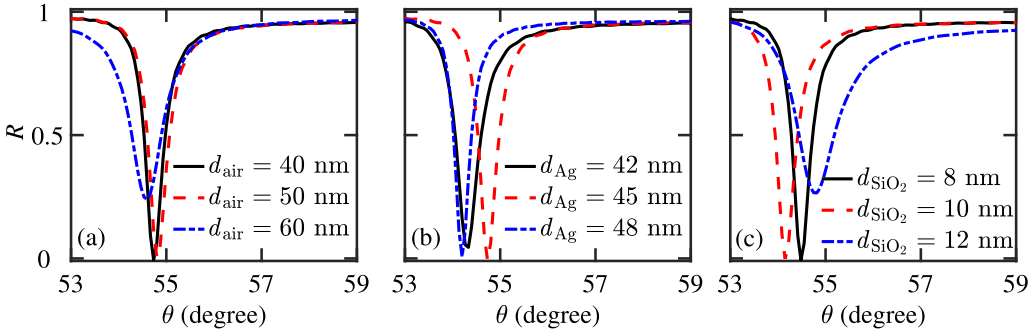

Fig. 2. R vs. θ of the proposed sensor for different thicknesses of (a) air gap, (b) Ag, and (c) SiO_2. In these studies, $n_s = 1.3323$.

Table 1
Refractive indices and thicknesses of different layers of the proposed glucose sensor. The refractive indices are for a 633-nm incident light.

Material	Refractive index	Thickness (nm)
BK7	1.515	Semi-infinite
Air	1.00	40
Ag	Real: 0.055 Imag: 4.285	45
h-BN	1.670	1
Graphene	V_g-dependent	0.34
SiO_2	1.460	8
Si	3.881	50
Blood sample	Concentration-dependent	100

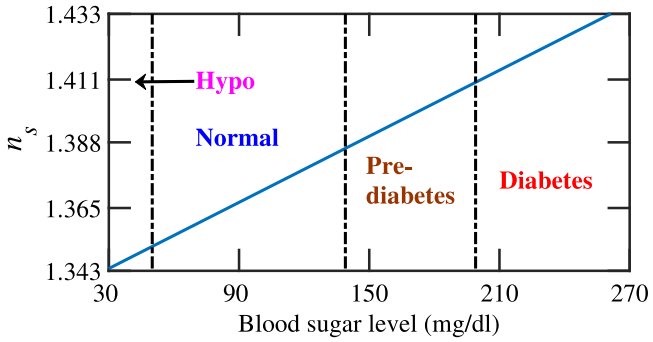

Fig. 3. Refractive index of the blood sample (n_s) as a function of blood sugar level.

published literature [47–49]. The refractive indices and thicknesses for different layers of the proposed structure are given in Table 1.

The complex refractive index of graphene will depend on several operating parameters, especially on the applied control voltage across it. Therefore, the calculation of graphene refractive index requires a special treatment. The complex permittivity of a two-dimensional (2-D) mono-layer graphene sheet can be given by [50]

$$\varepsilon(\omega) = 1 + i\frac{\sigma}{\omega\varepsilon_0 t}, \tag{1}$$

where ε_0 is the permittivity of free space, ω is the angular frequency of the incident wave, σ is the conductivity, and t is the thickness of a graphene mono-layer. If ω and t are fixed, the permittivity of graphene basically depends on σ, which can be calculated using the so-called Kubo formula [51]

$$\sigma = i\frac{e^2 k_B T}{\pi\hbar^2(\omega + i\tau^{-1})}\left[\frac{E_f}{k_B T} + 2\ln\left(\exp\left(-\frac{E_f}{k_B T}\right) + 1\right)\right] + i\frac{e^2}{4\pi\hbar}\ln\left[\frac{2 \mid E_f \mid -\hbar(\omega + i\tau^{-1})}{2 \mid E_f \mid +\hbar(\omega + i\tau^{-1})}\right], \tag{2}$$

where k_B is the Boltzmann constant, $\hbar$ is the reduced Planck constant, e is the charge of an electron, and τ is the relaxation time of carriers in graphene that are excited due to the absorption of incident light. The first term on the right hand side of Eq. (2) is the conductivity that originates from intra-band carrier transitions due to light absorption, whereas the second term is the conductivity that originates from the inter-band carrier transitions.

The carrier relaxation time τ depends on E_f and Fermi velocity (V_f) by the following relation [52]

$$\tau = \frac{\mu E_f}{eV_f^2}, \tag{3}$$

where $V_f = 10^6$ m/s and E_f is related to n as $E_f = \hbar V_f(\pi n)^{1/2}$ [53]. Now, when there is a gate voltage applied between the graphene and Si layer of the proposed structure as shown in Fig. 1, n can be calculated using a parallel-plate capacitor model as [53]

$$n = \varepsilon_0\varepsilon_d\frac{V_g}{ed}, \tag{4}$$

where ε_d and d are the dielectric constant and the thickness of insulating SiO_2 layer, respectively. We note that E_f, and in turn, τ can be changed by V_g. Thus, V_g can be used to change the optical behavior of graphene. The carrier relaxation time also depends on mobility μ, which is related to n and temperature (T) given by [54]

$$\mu(n,T) = \frac{\mu_0}{1 + (n/n_{\text{ref}})^{\alpha}} \times \frac{1}{1 + (T/T_{\text{ref}} - 1)^{\beta}}, \tag{5}$$

where $\mu_0 = 230000$ cm^2 V^{-1} s^{-1}, $n_{\text{ref}} = 1.1\times10^{13}$ cm^{-2}, $T_{\text{ref}} = 300$ K, $\alpha = 2.2$, and $\beta = 3$, respectively [54,55]. In this work, we assume that the sensor is at room temperature, i.e., $T = 300$ K.

The optical property of blood, i.e., the refractive index of sample (n_s) will depend on the concentration of glucose mixed in it, and can be calculated as [15]

$$n_s = 0.000119 \times C + 1.33231, \tag{6}$$

where C is the density of glucose solution. A 10% (w/v) glucose solution is 10 g (w) glucose dissolved in 100 ml (v) water. The sugar level in blood sample (D) can be calculated by $D = C/M$ mg/dl, where M is the molar mass of glucose, which is 180.156 g/mol. We have calculated n_s using Eq. (6) for different BSLs, as shown in Fig. 3 [56]. The normal sugar level in blood is between 50 mg/dl to 139 mg/dl [57], which correspond to n_s from 1.3513 to 1.3864. A person is pre-diabetic if the BSL is between 140 mg/dl and 199 mg/dl, and diabetic if BSL $\geqslant$ 200 [57]. A BSL of $<$ 50 mg/dL is considered extremely low and alarming for human body [58]. In this work, we have chosen BSL from 30 mg/dl to 270 mg/dl to cover the entire BSL map that could be important to understand the performance of the proposed sensor.

3.2. Response to the incident light

To calculate the SPR dynamics of the proposed gate-controlled glucose sensor, we have solved 2-D full-field vectorial Maxwell's equations using the FDTD technique. The incidence angle of light has been varied to determine the reflection profile. To calculate the reflection profile,

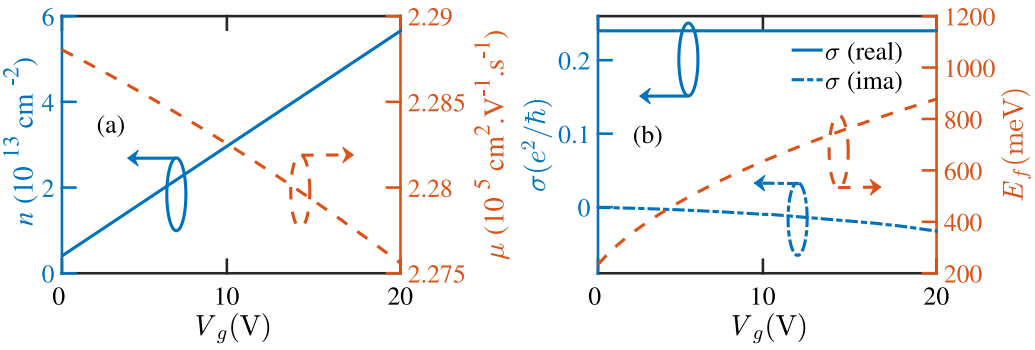

Fig. 4. (a) n and μ and (b) σ and E_f of a graphene mono-layer as functions of V_g. We assume $\epsilon_0 = 8.85\times10^{-12}$ F m^{-1}, $\epsilon_g = 3.9$, $d = 8$ nm, and $e = 1.6021 \times 10^{-19}$ C.

we have used TMM and considered the proposed structure an N-layer system, as shown in Fig. 1. For the incident transverse magnetic (TM) light, we can write [59]

$$R = | r_p |^2, \tag{7}$$

where r_p is the reflection coefficient for the TM-polarized incident light. We have calculated S of the proposed glucose sensor by [60]

$$S = \frac{\Delta\theta_r}{\Delta n_s}, \tag{8}$$

where $\Delta\theta_r$ is the change in resonance angle (θ_r) due to a change in the sample index Δn_s. FoM can be calculated by [61]

$$\text{FoM} = \frac{S}{\text{FWHM}}. \tag{9}$$

4. Simulation approach

In this work, 2-D FDTD simulations have been carried out to determine the dynamics of the incident light with the sensor. The simulation domain is 2000 nm in the y-direction, i.e., in the direction of the layer interfaces, and 6000 nm in the x-direction, i.e., in the direction perpendicular to the layer interfaces. A non-uniform meshing scheme has been employed in the simulation region to optimize the computational efficiency and precision of FDTD solutions by limiting the overall error caused by meshing to only < 0.05%. Additionally, a finer meshing is used in a smaller 600 nm × 300 nm region on the x-y plane centering the graphene and h-BN interface. In this fine meshing region, mesh-grids Δx = 0.1 nm and Δy = 0.2 nm have been chosen. The perfectly-matched layer (PML) boundary condition was used at the edges of the simulation region in the x-direction and Bloch boundary condition was used in the y-direction. The incident light has a 633-nm wavelength with TM polarization. The incidence angle has been varied from 45° to 70° to calculate the R profile. The incident light source is located at 3500 nm from the Air–Ag interface, whereas the detection plane of the reflected light is located at 3800 nm from the same interface.

5. Results and discussion

5.1. Sensor performance

To determine the performance of the proposed gate-controlled graphene SPR glucose sensor, we have assumed a pure graphene mono-layer in the sensor. The graphene mono-layer has $n = 1.08\times10^{13}$ cm^{-2}, E_f = 38.34 meV, and μ = 23 × 10^4 cm^2 V^{-1} s^{-1} when there is no applied V_g to it. We have varied V_g so that graphene parameters change, and so do the sensor performances. The results are presented for $V_g \le 20$ V, as thermally generated intrinsic carriers from graphene with $V_g > 20$ V may cause inaccurate results and a permanent fault in the structure [42,62]. Fig. 4 shows the properties of a graphene mono-layer as V_g varies from zero to 20 V. In Fig. 4(a), we find that n increases and μ decreases with the increase of V_g. In Fig. 4(b), we find that E_f increases as V_g increases since E_f is directly related to n. We have also calculated τ as V_g varies and found that τ increases as V_g increases. In particular, we find τ = 8.74, 11.42, 14.50, 17.05, and 19.97 ps when V_g = 0, 5, 10, 15, and 20 V, respectively.

Generally, the conductivity of graphene depends on both intra- and inter-band absorptions of the incident light. When the incident light wavelength is 633 nm, the incident photon energy $E_p > 2E_f$, and therefore, strong inter-band absorption occurs. However, E_f can be increased by applying V_g and the inter-band transitions with $E_p < 2E_f$ can be blocked due to Pauli blocking [63]. When $E_p < 2E_f$, intra-band absorption dominates, and graphene optical properties mainly depend on τ. Therefore, graphene optical properties can be changed by controlling V_g when $E_p < 2E_f$ [50]. In this work, the proposed sensor has been designed for $E_p < 2E_f$ to control the graphene optical properties by controlling V_g. Fig. 4(b) shows both real and imaginary parts of σ of a graphene mono-layer as functions of V_g. We note that the real part of σ does not vary as V_g increases. By contrast, the imaginary part of σ gradually decreases as V_g increases from zero to 20 V. Mono-layer graphene supports TM plasmons from terahertz (THz) to mid-infrared (MIR) wavelength range, although transverse electric (TE) plasmons can be excited up to visible wavelength. When V_g increases, E_f increases as well. Therefore, TM plasmons of mono-layer graphene can be obtained at 633 nm wavelength. A similar trend is observed for intra-band absorption from THz to MIR range [64,65]. As a result, the incident light is strongly absorbed in the graphene mono-layer of our designed sensor. The complex refractive index of a graphene mono-layer has been calculated from σ, as given in Eq. (1), to be used in FDTD simulations.

Fig. 5(a) shows R as a function of θ for five different values of V_g. Here, the sample has a BSL = 78.60 mg/dl, which corresponds to n_s = 1.3625. Since the light absorption by graphene increases with V_g, R decreases with V_g. The absorption of incident light increases by 16.88% when V_g increases from zero to 20 V. We note that θ_r increases with V_g. The changes of θ_r and R with V_g have a significant impact on the sensor performance parameters.

Fig. 5(b) shows the FWHM of R profile of the proposed glucose sensor for different V_g when the BSL varies from 30 mg/dl to 270 mg/dl. We note that FWHM of R increases as the BSL increases. The excited SPPs decay at a faster rate when BSL increases as n_s increases with BSL. As a result, the FWHM of the R profile increases. By contrast, FWHM of the R profile decreases as V_g increases. A smaller FWHM will decrease the spectral noise and increase the signal-to-noise ratio (SNR) of the detected signal. When V_g increases, the graphene mono-layer strongly confines the incident light, and we find that the FWHM of the R profile decreases.

Fig. 6(a) shows S of the proposed gate-controlled graphene SPR glucose sensor as a function of the BSL. We note that S increases as BSL increases and reaches 108 degree/RIU for V_g = 20 V and BSL is 270 mg/dl. We also note that S increases as V_g increases. Notably, S increases by 21.48% when V_g increases from zero to 20 V for a BSL

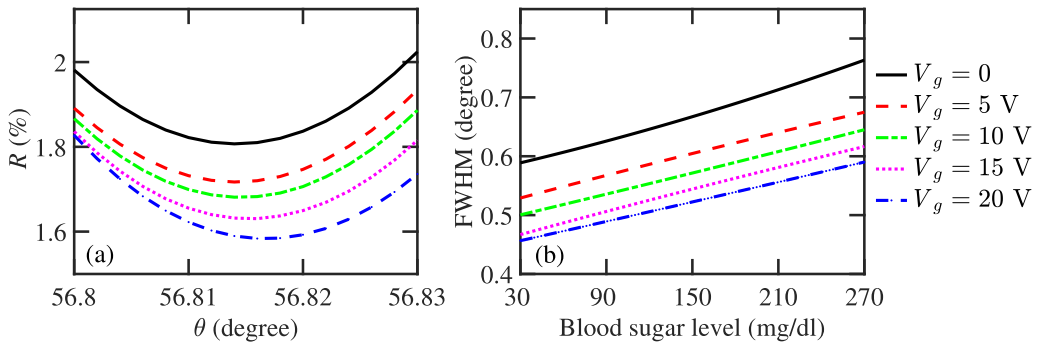

Fig. 5. (a) R as a function of θ and (b) FWHM of the R profile as a function of the BSL of the proposed gate-controlled graphene SPR glucose sensor for different V_g. To calculate R profile, we assume $n_s = 1.3625$, which corresponds to a BSL of 78.60 mg/dl.

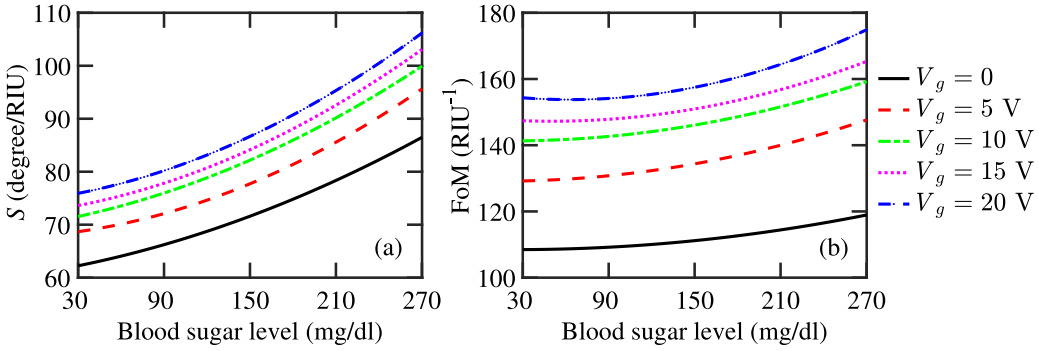

Fig. 6. (a) S and (b) FoM as functions of BSL of the proposed glucose sensor for different V_g.

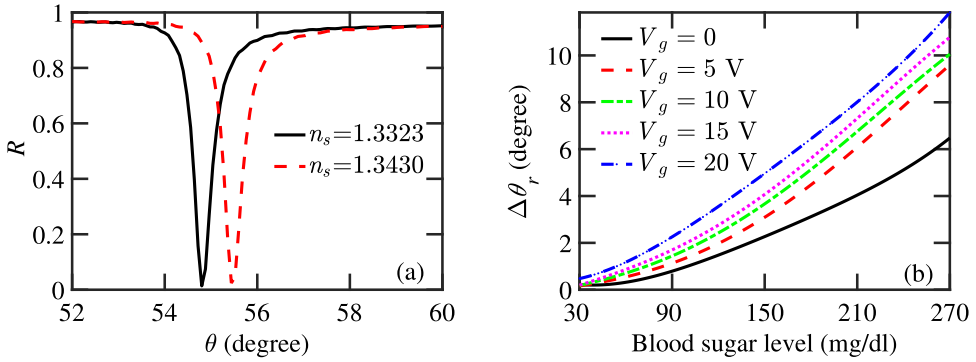

Fig. 7. (a) R profile as a function of θ and (b) $\Delta\theta_r$ as functions of BSL and V_g for the proposed glucose sensor.

of 270 mg/dl. As S depends on the change of θ_r and a greater V_g shows a greater change in θ_r, we find that S increases as V_g increases. In Fig. 6(b), we show FoM as a function of the BSL for different gate voltages. We note that FoM increases with the increase of both BSL and V_g. When $V_g = 20$ V, the maximum FoM is 178 RIU^{-1} at 270 mg/dl BSL. We note that FoM increases by 49.57% when V_g increases from zero to 20 V in the range of BSL considered in this work. As the negative value of imaginary σ increases with the increase of V_g, a mono-layer graphene absorbs more light as V_g increases. Therefore, FoM increases as V_g increases.

The change in θ_r, i.e., $\Delta\theta_r$, in the R profile with the change in BSL represents the selectivity of an SPR sensor [66]. Fig. 7(a) shows R as a function of θ for two different n_s when $V_g = 0$. The first resonance is observed at 54.80° when $n_s = 1.3323$, which corresponds to zero BSL. The second resonance is observed at 55.24° when $n_s = 1.3430$, which corresponds to 30 mg/dl BSL. In Fig. 7(a), $\Delta\theta_r = 0.44°$ when $V_g = 0$. By contrast, Fig. 7(b) shows $\Delta\theta_r$ with the change of BSL at different V_g. We find that the sensor becomes more selective when BSL and V_g increase. The increase of $\Delta\theta_r$ with BSL implies that the proposed sensor has affinity toward glucose.

We find that the calculated S and FoM of the proposed sensor are much greater than that of the state-of-the-art optical sensors in the detection of BSL. In Table 2, we compare S and FoM of our proposed glucose sensor with several recently proposed sensors that use graphene in the structure. The wavelength of the incident light is 633 nm in all cases presented in Table 2. Also, only a graphene mono-layer is used in all cases, except in Ref. [32], where 13 layers of graphene are used. In this work, the S and FoM have been calculated for the sensing layer refractive indices 1.343–1.433, which correspond to 30–270 mg/dl BSL. The maximum S and FoM of the proposed sensor are obtained when the sensing layer index is 1.433. In Table 2, the S and

Table 2
Performance comparison of our proposed sensor with several recently proposed graphene-based sensors.

Sensor configuration	n_s	S (degree/RIU)	FoM (RIU^{-1})	Reference
SF10/ZnO/Au/MoS_2/graphene/sample	1.330–1.450	101.58	15.11	[32]
SF10/Au/WS_2/graphene/sample	1.400	95.71	25.19	[33]
BK7/Ag/graphene/sample	1.330–1.370	91.76	52.31	[67]
SF10/Cr/Ag/graphene/affinity/sample	1.432	61.54	8.90	[68]
This work	1.343–1.433	108.00	178.00	–

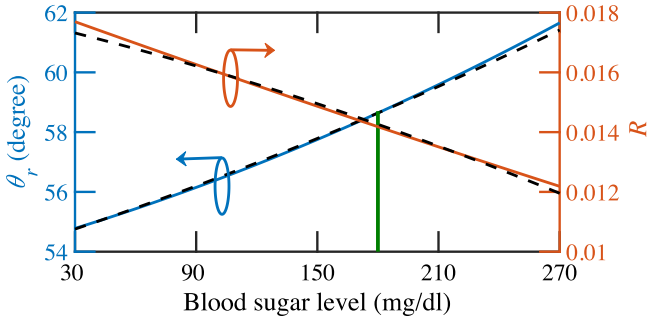

Fig. 8. Simulation results of θ_r and R vs. BSL (dashed lines), and regression lines of θ_r and R vs. BSL (solid lines). The solid green line determines 180 mg/dl BSL, when measured $\theta_r = 58.8°$ or $R = 0.01425$. We assume $V_g = 20$ V.

FoM of the proposed sensor are compared with that of the sensors, which report results with a sensing layer index close to 1.433.

5.2. Measurement accuracy

Accuracy is a key performance parameter for a sensor in the detection of the BSL. The parameters R and θ_r can be used individually or simultaneously in the proposed sensor to detect and measure the BSL precisely. The determination of the BSL using θ_r and R simultaneously will be more precise, however, with an increase in the complexity of the measurement technique. Fig. 8 shows the dependence of R and θ_r on BSL when $V_g = 20$ V. Fig. 8 also shows linear regression lines drawn for the relations θ_r vs. BSL and R vs. BSL. The regression lines $y = a+bx$ have been determined for both θ_r vs. BSL and R vs. BSL relations, where a is the intercept on the y-axis, b is the slope, x is the BSL, and y is either θ_r or R, respectively [69]. We find that the BSL estimated by θ_r provides a better accuracy than that estimated by R as the regression line for θ_r fits better with the simulated values. Notably, the coefficient of determination (R^2) is 96.50% for the linear regression line for θ_r, while 94.11% for the linear regression line for R. The linear regression lines can be used as a reference to detect the BSL for the proposed sensor. For example, when measured $\theta_r = 58.80°$, we can decide that the BSL is 180 mg/dl using the reference regression line for θ_r.

5.3. Effects of temperature

The accuracy of a glucose sensor depends on many factors, including the strip manufacturing process, chemical stability of enzyme, sample collection method, sample amount, and most importantly the temperature at which the measurement takes place. We have analyzed the effects of temperature on the detection of BSL by the proposed sensor. In the analysis, we have assumed $T = 25$ °C as a reference temperature and varied it by a maximum $\Delta T = \pm 10$ °C.

Optical properties of layers of the proposed sensor, except for the Ag layer, do not significantly depend on temperature, especially at the incident 633 nm wavelength and in the temperature range around 25 °C. In particular, the change of the refractive indices of BK7, h-BN, SiO_2, and Si due to the change in temperature is negligible in the visible wavelength range [70–73]. Therefore, in the range $T = 15$–35 °C, the change in optical properties of most layers of the proposed sensor is negligible.

The temperature dependence of the optical property of graphene is a little more complicated due to its unique properties. The effect of temperature on the optical property of graphene will depend on μ and τ, and hence, σ. Since the temperature dependence of the optical property of graphene is not well-studied and not available in the literature, we have calculated it in this work. In Fig. 9, we show μ vs. temperature, and τ vs. temperature for a graphene mono-layer calculated using Eq. (5). We find that both μ and τ do not vary with temperature when V_g remains fixed. We note that the work function and E_f of a graphene mono-layer do not depend on temperature as well [74]. As a result, σ, and hence, the optical property of a graphene mono-layer does not change with temperature for the cases considered in this work.

Therefore, the temperature-sensitive performance of the proposed sensor will depend only on the temperature-dependent optical property of Ag. We use the Drude–Lorentz model to calculate the temperature-dependent optical property of Ag, i.e., the effect of temperature on the dielectric constant of Ag. The expression of ε of Ag is given by [46]

$$\varepsilon = 1 - \frac{\omega_p^2}{\omega(\omega + i\omega_c)}, \tag{10}$$

where ω_p and ω_c are the plasma and collision frequencies, respectively. The collision or scattering frequency ω_c depends on temperature and can be written as [75]

$$\omega_c = \omega_{ce} + \omega_{cp}, \tag{11}$$

where ω_{ce} and ω_{cp} are the electron–electron and electron–phonon scattering frequencies in Ag. The temperature dependence of ω_{ce} can be described by the Lawrence model [76]

$$\omega_{ce} = \frac{\pi^3 \Gamma \Delta}{12\hbar E_f}\left[(k_B T)^2 + \left(\frac{\hbar\omega}{2\pi}\right)^2\right], \tag{12}$$

where Δ is the fractional scattering and Γ is the Fermi-surface average of the scattering probability. We assume $\Delta = 0.75$ and $\Gamma = 0.55$ [76]. The temperature dependence of ω_{cp} can be described using the Holstein's model [77]

$$\omega_{cp} = \omega_0\left[\frac{2}{5} + \frac{4T^5}{\Theta_D^5}\int_0^{\Theta_D/T}\frac{Z^4}{e^Z - 1}\mathrm{dZ}\right], \tag{13}$$

where Θ_D is the Debye temperature, Z is the quasi-particle weight, and ω_0 is a constant [78]. We have used $\Theta_D = 227.3$ K, $Z = 0.8$, and $\omega_0 = 0.05$ [78]. Lastly, ω_p has been calculated using [79]

$$\omega_p = \sqrt{\frac{4\pi N e^2}{m}}, \tag{14}$$

where m is the effective mass of an electron and N is the density of conduction electrons.

The optical property of the blood sample also depends on temperature. The temperature-dependent n_s can be obtained using [80]

$$n_s = 1.3356 + (1.5333\times10^{-3})\times C - (9.0\times10^{-5})\times C^2 - (1.2647\times10^{-4})\times(T - 273.15) - (4.0\times10^{-8})\times(T - 273.15)^2. \tag{15}$$

To determine the temperature-dependent measurement error for the proposed sensor, we have considered two cases: (i) First, we have assumed that only the sensor temperature varies while the sample temperature remains fixed and (ii) Second, we have assumed that the sensor and sample temperatures are equal and vary simultaneously.

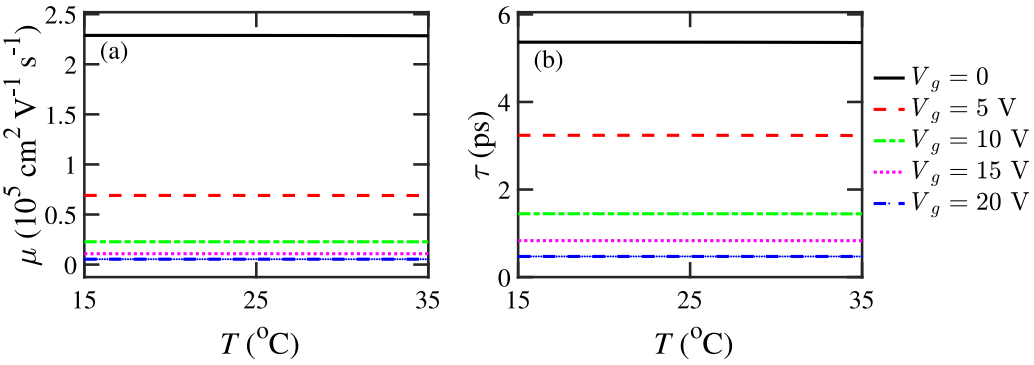

Fig. 9. Effects of T on graphene (a) μ, and (b) τ for five different V_g.

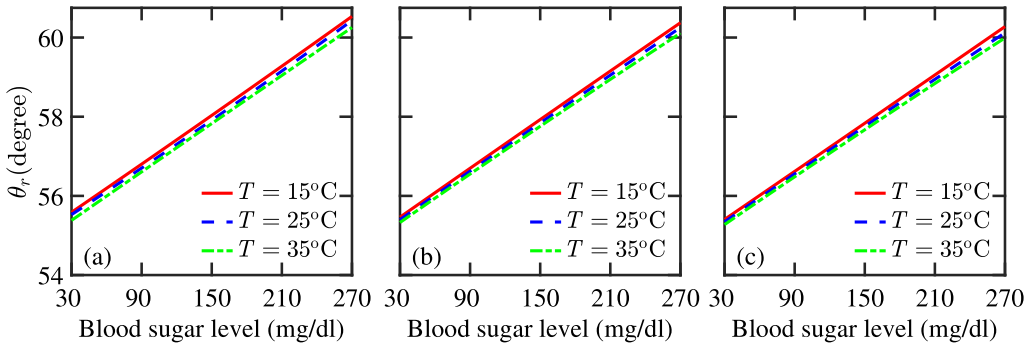

Fig. 10. θ_r vs. BSL of the proposed sensor for different sensor temperature. We assume that the sample temperature remains fixed at (a) 15 °C, (b) 25 °C, and (c) 35 °C.

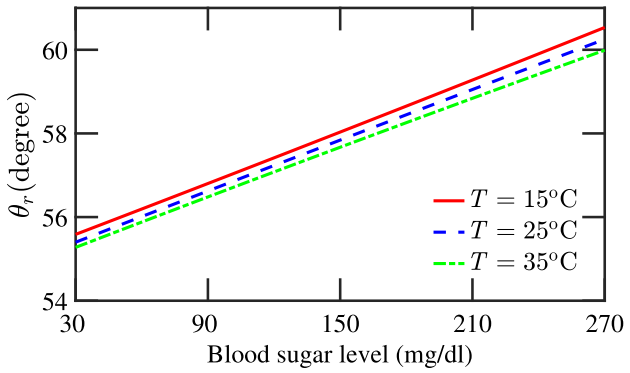

Fig. 11. θ_r vs. BSL for different temperatures (T) of the sensor and sample layer. The sensor and sample layer temperatures are equal and they vary simultaneously.

Table 3
Maximum measurement error and average error of detected BSL when sensor T is varying from 25 °C for different n_s temperature.

Sample temperature (°C)	Sensor temperature variation (ΔT, °C)	Maximum %Error	Average %Error
15	10	7.12	3.70
	5	3.56	2.05
	−5	−3.52	−1.72
	−10	−7.06	−3.51
25	10	4.70	2.97
	5	3.72	1.70
	−5	−3.24	−1.70
	−10	−3.86	−2.55
35	10	3.40	2.90
	5	3.32	1.74
	−5	−3.46	−1.81
	−10	−4.02	−2.61

While the first case signifies the temperature-sensitive performance of the proposed sensor, the second case helps us know the performance in an actual condition. Fig. 10 shows θ_r vs. BSL for three different temperatures of the sensor. The sample temperature is kept fixed at 15 °C, 25 °C, and 35 °C in Figs. 10(a), 10(b), and 10(c), respectively. We find that while θ_r increases when the sensor temperature decreases, θ_r decreases when the sensor temperature increases.

The percentage error in the detection of BSL is calculated using the following equation

$$\%\text{Error} = \frac{\text{BSL}_{25\ ^\circ\text{C}} - \text{BSL}_{T_{\text{diff}}^\circ\text{C}}}{\text{BSL}_{25\ ^\circ\text{C}}} \times 100, \tag{16}$$

where T_{diff}°C is the temperature at which the BSL is calculated. The maximum and average calculated %Error for the cases presented in Fig. 10 are given in Table 3. We note that the maximum error is 7.12% when the sensor temperature varies by 10 °C and the sample temperature is 15 °C. We also note that the average error of our proposed sensor remains < 4% for a $\Delta T = \pm 10$ °C.

Next, we present results when both the sensor and sample layer have the same temperature. Fig. 11 shows the effects of temperature on θ_r of the proposed glucose sensor as the temperatures of the sensor and sample layer change simultaneously. We note that the effects of temperature become more pronounced as the glucose level increases. We find a maximum error of 7.40% when the temperature varies by −10 °C, i.e., when T = 15 °C. In Table 4, we show the error in the detection of the BSL due to temperature changes of the sensor and the sample. Notably, the absolute value of the average error remains <5%.

6. Conclusion

We have proposed a label-free graphene SPR sensor that shows a tunable optical property with the applied gate voltage. The proposed

Table 4
Maximum and average %Error of the calculated BSL when both the sensor and sample temperatures vary.

ΔT (°C)	Maximum %Error	Average %Error
10	6.44	3.66
5	3.68	2.34
−5	−4.08	−2.26
−10	−7.40	−4.75

glucose sensor offers enhanced performances compared to state-of-the-art graphene-based optical sensors. The proposed sensor performances increase as the applied gate voltage increases. The sensor can detect and measure the BSL with high precision either using the resonance angle or the reflection profile. Since our proposed sensor detects BSL without using labels and does not require chemical enzymes, the environmental factors do not have any lasting effect on the performance, except for the temperature-induced index variation of metal at the moment of measurement. However, the change in temperature by ±10 °C around room temperature affects the detection accuracy by only < 5%.

Declaration of competing interest

The authors declare that they have no known competing financial interests or personal relationships that could have appeared to influence the work reported in this paper.

Funding

This research did not receive any specific grant from funding agencies in the public, commercial, or not-for-profit sectors.

References

[1] I.D. Federation, 9th edition of the diabetes atlas 2019, 2020, (Accessed 10 June 2020).
[2] S. Haxha, J. Jhoja, Optical based noninvasive glucose monitoring sensor prototype, IEEE Photonics J. 8 (6) (2016) 1–11.
[3] S.K. Srivastava, R. Verma, B.D. Gupta, Surface plasmon resonance based fiber optic glucose biosensor, in: Third Asia Pacific Optical Sensors Conference, International Society for Optics and Photonics, 2012, 8351, p. 83511Z.
[4] J. Dyro, Clinical Engineering HandBook, Elsevier, 2004.
[5] E.-H. Yoo, S.-Y. Lee, Glucose biosensors: an overview of use in clinical practice, Sensors 10 (5) (2010) 4558–4576.
[6] F.D.A. USA, blood glucose meter accuracy 2014, 2020, (Accessed 10 June 2020).
[7] K. Tonyushkina, J.H. Nichols, Glucose meters: a review of technical challenges to obtaining accurate results, J. Diabetes Sci. Technol. 3 (4) (2009) 971–980.
[8] C. Li, S. Xu, J. Yu, Z. Li, W. Li, J. Wang, A. Liu, B. Man, S. Yang, C. Zhang, Local hot charge density regulation: Vibration-free pyroelectric nanogenerator for effectively enhancing catalysis and in-situ surface enhanced raman scattering monitoring, Nano Energy 81 (2021) 105585.
[9] C. Zhang, C. Li, J. Yu, S. Jiang, S. Xu, C. Yang, Y.J. Liu, X. Gao, A. Liu, B. Man, Sers activated platform with three-dimensional hot spots and tunable nanometer gap, Sensors Actuators B 258 (2018) 163–171.
[10] X. Zhao, C. Liu, J. Yu, Z. Li, L. Liu, C. Li, S. Xu, W. Li, B. Man, C. Zhang, Hydrophobic multiscale cavities for high-performance and self-cleaning surface-enhanced raman spectroscopy (sers) sensing, Nanophotonics 9 (16) (2020) 4761–4773.
[11] J. Yu, M. Yang, Z. Li, C. Liu, Y. Wei, C. Zhang, B. Man, F. Lei, Hierarchical particle-in-quasicavity architecture for ultratrace in situ raman sensing and its application in real-time monitoring of toxic pollutants, Anal. Chem. 92 (21) (2020) 14754–14761.
[12] M.M. Hossain, M.A. Talukder, Optical magnetism in surface plasmon resonance–based sensors for enhanced performance, Plasmonics (2020) 1–8.
[13] E. D'costa, I. Higgins, A. Turner, Quinoprotein glucose dehydrogenase and its application in an amperometric glucose sensor, Biosensors 2 (2) (1986) 71–87.
[14] S. Shtelzer, S. Braun, An optical biosensor based upon glucose oxidase immobilized in sol–gel silicate matrix, Biotechnol. Appl. Biochem. 19 (3) (1994) 293–305.
[15] X. Yang, Y. Lu, M. Wang, J. Yao, A photonic crystal fiber glucose sensor filled with silver nanowires, Opt. Commun. 359 (2016) 279–284.
[16] H. Thenmozhi, M.M. Rajan, V. Devika, D. Vigneswaran, N. Ayyanar, D-glucose sensor using photonic crystal fiber, Optik 145 (2017) 489–494.
[17] S. Yang, Y. Zhang, X. Peng, Y. Lu, S. Xie, J. Li, W. Chen, Z. Jiang, J. Peng, H. Li, Theoretical study and experimental fabrication of high negative dispersion photonic crystal fiber with large area mode field, Opt. Express 14 (7) (2006) 3015–3023.
[18] H. Vahed, C. Nadri, Sensitivity enhancement of spr optical biosensor based on graphene–mos2 structure with nanocomposite layer, Opt. Mater. 88 (2019) 161–166.
[19] P.S. Menon, F.A. Said, G.S. Mei, D.D. Berhanuddin, A.A. Umar, S. Shaari, B.Y. Majlis, Urea and creatinine detection on nano-laminated gold thin film using kretschmann-based surface plasmon resonance biosensor, PLoS One 13 (7) (2018).
[20] H.H. Nguyen, J. Park, S. Kang, M. Kim, Surface plasmon resonance: a versatile technique for biosensor applications, Sensors 15 (5) (2015) 10481–10510.
[21] W. Lam, L. Chu, C. Wong, Y. Zhang, A surface plasmon resonance system for the measurement of glucose in aqueous solution, Sensors Actuators B 105 (2) (2005) 138–143.
[22] P.S. Menon, B. Mulyanti, N.A. Jamil, C. Wulandari, H.S. Nugroho, G.S. Mei, N.F.Z. Abidin, L. Hasanah, R.E. Pawinanto, D.D. Berhanuddin, Refractive index and sensing of glucose molarities determined using au-cr k-spr at 670/785 nm wavelength, Sains Malaysiana 48 (6) (2019) 1259–1265.
[23] P. Sun, M. Wang, L. Liu, L. Jiao, W. Du, F. Xia, M. Liu, W. Kong, L. Dong, M. Yun, Sensitivity enhancement of surface plasmon resonance biosensor based on graphene and barium titanate layers, Appl. Surf. Sci. 475 (2019) 342–347.
[24] H. Jiang, S. Choudhury, Z.A. Kudyshev, D. Wang, L.J. Prokopeva, P. Xiao, Y. Jiang, A.V. Kildishev, Enhancing sensitivity to ambient refractive index with tunable few-layer graphene/hbn nanoribbons, Photonics Research 7 (7) (2019) 815–822.
[25] S. Chen, C. Lin, Figure of merit analysis of graphene based surface plasmon resonance biosensor for visible and near infrared, Opt. Commun. 435 (2019) 102–107.
[26] N.N.M. Rosddi, Y.W. Fen, N.A.A. Anas, N.A.S. Omar, N.S.M. Ramdzan, W.M.E.M.M. Daniyal, Cationically modified nanocrystalline cellulose/carboxyl-functionalized graphene quantum dots nanocomposite thin film: Characterization and potential sensing application, Crystals 10 (10) (2020) 875.
[27] A. Panda, P.D. Pukhrambam, G. Keiser, Performance analysis of graphene-based surface plasmon resonance biosensor for blood glucose and gas detection, Appl. Phys. A 126 (3) (2020) 1–12.
[28] N. Mudgal, A. Saharia, A. Agarwal, J. Ali, P. Yupapin, G. Singh, Modeling of highly sensitive surface plasmon resonance (spr) sensor for urine glucose detection, Opt. Quantum Electron. 52 (2020) 1–14.
[29] K.V. Sreekanth, S. Zeng, J. Shang, K.-T. Yong, T. Yu, Excitation of surface electromagnetic waves in a graphene-based bragg grating, Sci. Rep. 2 (737) (2012).
[30] X. Zhu, W. Yan, P. Uhd Jepsen, O. Hansen, N. Asger Mortensen, S. Xiao, Experimental observation of plasmons in a graphene monolayer resting on a two-dimensional subwavelength silicon grating, Appl. Phys. Lett. 102 (13) (2013) 131101.
[31] P. Alonso-González, A.Y. Nikitin, F. Golmar, A. Centeno, A. Pesquera, S. Vélez, J. Chen, G. Navickaite, F. Koppens, A. Zurutuza, et al., Controlling graphene plasmons with resonant metal antennas and spatial conductivity patterns, Science 344 (6190) (2014) 1369–1373.
[32] A.S. Kushwaha, A. Kumar, R. Kumar, S. Srivastava, A study of surface plasmon resonance (spr) based biosensor with improved sensitivity, Photon. Nanostruct.: Fundam. Appl. 31 (2018) 99–106.
[33] M.S. Rahman, M.R. Hasan, K.A. Rikta, M. Anower, A novel graphene coated surface plasmon resonance biosensor with tungsten disulfide (WS_2) for sensing DNA hybridization, Opt. Mater. 75 (2018) 567–573.
[34] S. Zeng, S. Hu, J. Xia, T. Anderson, X.-Q. Dinh, X.-M. Meng, P. Coquet, K.-T. Yong, Graphene–MoS_2 hybrid nanostructures enhanced surface plasmon resonance biosensors, Sensors Actuators B 207 (2015) 801–810.
[35] B. Deng, Q. Guo, C. Li, H. Wang, X. Ling, D.B. Farmer, S.-j. Han, J. Kong, F. Xia, Coupling-enhanced broadband mid-infrared light absorption in graphene plasmonic nanostructures, ACS Nano 10 (12) (2016) 11172–11178.
[36] Z. Yu, S. Fan, Extraordinarily high spectral sensitivity in refractive index sensors using multiple optical modes, Opt. Express 19 (11) (2011) 10029–10040.
[37] Y. Kaneoka, K. Nishigaki, Y. Mizutani, T. Iwata, Precise measurement of the thickness of a dielectric layer on a metal surface by use of a modified otto optical configuration, Int. J. Optomechatronics 9 (1) (2015) 48–61.
[38] B. Yektaparast, H. Shirkani, Controlling optical absorption of graphene in near-infrared region by surface plasmons, Plasmonics 13 (5) (2018) 1623–1630.
[39] C.R. Dean, A.F. Young, I. Meric, C. Lee, L. Wang, S. Sorgenfrei, K. Watanabe, T. Taniguchi, P. Kim, K.L. Shepard, et al., Boron nitride substrates for high-quality graphene electronics, Nature Nanotechnol. 5 (10) (2010) 722.
[40] A. Woessner, M.B. Lundeberg, Y. Gao, A. Principi, P. Alonso-González, M. Carrega, K. Watanabe, T. Taniguchi, G. Vignale, M. Polini, et al., Highly confined low-loss plasmons in graphene–boron nitride heterostructures, Nature Mater. 14 (4) (2015) 421.
[41] J. Hu, Y. Qing, S. Yang, Y. Ren, X. Wu, W. Gao, C. Wu, Tailoring total absorption in a graphene monolayer covered subwavelength multilayer dielectric grating structure at near-infrared frequencies, J. Opt. Soc. Amer. B 34 (4) (2017) 861–868.

[42] Y. Yin, Z. Cheng, L. Wang, K. Jin, W. Wang, Graphene, a material for high temperature devices–intrinsic carrier density, carrier drift velocity, and lattice energy, Sci. Rep. 4 (5758) (2014).
[43] M. Kim, C.Y. Jeong, H. Heo, S. Kim, Optical reflection modulation using surface plasmon resonance in a graphene-embedded hybrid plasmonic waveguide at an optical communication wavelength, Opt. Lett. 40 (6) (2015) 871–874.
[44] C.-W. Lin, K.-P. Chen, C.-N. Hsiao, S. Lin, C.-K. Lee, Design and fabrication of an alternating dielectric multi-layer device for surface plasmon resonance sensor, Sensors Actuators B 113 (1) (2006) 169–176.
[45] G. Lan, S. Liu, Y. Ma, X. Zhang, Y. Wang, Y. Song, Sensitivity and figure-of-merit enhancements of liquid-prism spr sensor in the angular interrogation, Opt. Commun. 352 (2015) 49–54.
[46] P.K. Maharana, T. Srivastava, R. Jha, On the performance of highly sensitive and accurate graphene-on-aluminum and silicon-based spr biosensor for visible and near infrared, Plasmonics 9 (5) (2014) 1113–1120.
[47] S.Z. Uddin, M.A. Talukder, Two-dimensional materials for improved resolution in total internal reflection fluorescence microscopy, Mater. Res. Express 4 (9) (2017) 096203.
[48] P.R. Gray, P. Hurst, R.G. Meyer, S. Lewis, Analysis and Design of Analog Integrated Circuits, Wiley, 2001.
[49] E.D. Palik, HandBook of Optical Constants of Solids, vol. 3, Academic press, 1998.
[50] A. Al Sayem, M.R.C. Mahdy, I. Jahangir, M.S. Rahman, Ultrathin ultra-broadband electro-absorption modulator based on few-layer graphene based anisotropic metamaterial, Opt. Commun. 384 (2017) 50–58.
[51] Q. Bao, H. Zhang, B. Wang, Z. Ni, C.H.Y.X. Lim, Y. Wang, D.Y. Tang, K.P. Loh, Broadband graphene polarizer, Nature Photon. 5 (7) (2011) 411.
[52] H. Lu, C. Zeng, Q. Zhang, X. Liu, M.M. Hossain, P. Reineck, M. Gu, Graphene-based active slow surface plasmon polaritons, Sci. Rep. 5 (8443) (2015).
[53] W. Gao, J. Shu, C. Qiu, Q. Xu, Excitation of plasmonic waves in graphene by guided-mode resonances, ACS Nano 6 (9) (2012) 7806–7813.
[54] V.E. Dorgan, M.-H. Bae, E. Pop, Mobility and saturation velocity in graphene on SiO_2, Appl. Phys. Lett. 97 (8) (2010) 082112.
[55] K.I. Bolotin, K.J. Sikes, Z. Jiang, M. Klima, G. Fudenberg, J. Hone, P. Kim, H. Stormer, Ultrahigh electron mobility in suspended graphene, Solid State Commun. 146 (9–10) (2008) 351–355.
[56] N.I. of diabetes, digestive, and k. diseases, diabetes, 2020, 2020, (Accessed 10 June 2020).
[57] P.H. Marathe, H.X. Gao, K.L. Close, American diabetes association standards of medical care in diabetes 2017, J. Diabetes 9 (4) (2017) 320–324.
[58] P.E. Cryer, L. Axelrod, A.B. Grossman, S.R. Heller, V.M. Montori, E.R. Seaquist, F.J. Service, Evaluation and management of adult hypoglycemic disorders: an endocrine society clinical practice guideline, J. Clin. Endocrinol. Metab. 94 (3) (2009) 709–728.
[59] J. Yan, K.S. Thygesen, K.W. Jacobsen, Nonlocal screening of plasmons in graphene by semiconducting and metallic substrates: first-principles calculations, Phys. Rev. Lett. 106 (14) (2011) 146803.
[60] B. Lahiri, S.G. McMeekin, M. Richard, N.P. Johnson, Enhanced fano resonance of organic material films deposited on arrays of asymmetric split-ring resonators (a-SRRs), Opt. Express 21 (8) (2013) 9343–9352.
[61] L. Tong, H. Wei, S. Zhang, H. Xu, Recent advances in plasmonic sensors, Sensors 14 (5) (2014) 7959–7973.
[62] Z. Cheng, Q. Zhou, C. Wang, Q. Li, C. Wang, Y. Fang, Toward intrinsic graphene surfaces: a systematic study on thermal annealing and wet-chemical treatment of SiO_2-supported graphene devices, Nano Lett. 11 (2) (2011) 767–771.
[63] Q. Bao, H. Zhang, Y. Wang, Z. Ni, Y. Yan, Z.X. Shen, K.P. Loh, D.Y. Tang, Atomic-layer graphene as a saturable absorber for ultrafast pulsed lasers, Adv. Funct. Mater. 19 (19) (2009) 3077–3083.
[64] S.G. Menabde, D.R. Mason, E.E. Kornev, C. Lee, N. Park, Direct optical probing of transverse electric mode in graphene, Sci. Rep. 6 (21523) (2016).
[65] G.W. Hanson, Dyadic Green's functions and guided surface waves for a surface conductivity model of graphene, J. Appl. Phys. 103 (6) (2008) 064302.
[66] N.A.S. Omar, Y.W. Fen, J. Abdullah, A.R. Sadrolhosseini, Y. Mustapha Kamil, N.M. Fauzi, H.S. Hashim, M.A. Mahdi, Quantitative and selective surface plasmon resonance response based on a reduced graphene oxide–polyamidoamine nanocomposite for detection of dengue virus e-proteins, Nanomaterials 10 (3) (2020) 569.
[67] P.K. Maharana, P. Padhy, R. Jha, On the field enhancement and performance of an ultra-stable spr biosensor based on graphene, IEEE Photonics Technol. Lett. 25 (22) (2013) 2156–2159.
[68] A. Verma, A. Prakash, R. Tripathi, Sensitivity enhancement of surface plasmon resonance biosensor using graphene and air gap, Opt. Commun. 357 (2015) 106–112.
[69] K.H. Zou, K. Tuncali, S.G. Silverman, Correlation and simple linear regression, Radiology 227 (3) (2003) 617–628.
[70] M. Englert, P. Hartmann, S. Reichel, Optical glass: refractive index change with wavelength and temperature, in: Optical Modelling and Design III, International Society for Optics and Photonics, 2014, 9131, p. 91310H.
[71] D. Jin-Xiang, Z. Xiao-Kang, Y. Qian, W. Xu-Yang, C. Guang-Hua, H. De-Yan, Optical properties of hexagonal boron nitride thin films deposited by radio frequency bias magnetron sputtering, Chin. Phys. B 18 (9) (2009) 4013.
[72] J. Matsuoka, N. Kitamura, S. Fujinaga, T. Kitaoka, H. Yamashita, Temperature dependence of refractive index of SiO_2 glass, J. Non-Cryst. Solids 135 (1) (1991) 86–89.
[73] G. Jellison Jr, F. Modine, Optical functions of silicon at elevated temperatures, J. Appl. Phys. 76 (6) (1994) 3758–3761.
[74] F. Zhu, X. Lin, P. Liu, K. Jiang, Y. Wei, Y. Wu, J. Wang, S. Fan, Heating graphene to incandescence and the measurement of its work function by the thermionic emission method, Nano Res. 7 (4) (2014) 553–560.
[75] K. Ujihara, Reflectivity of metals at high temperatures, J. Appl. Phys. 43 (5) (1972) 2376–2383.
[76] W. Lawrence, Electron–electron scattering in the low-temperature resistivity of the noble metals, Phys. Rev. B 13 (12) (1976) 5316.
[77] T. Holstein, Optical and infrared volume absorptivity of metals, Phys. Rev. 96 (2) (1954) 535.
[78] D. Meyer, A. Hewson, R. Bulla, Gap formation and soft phonon mode in the Holstein model, Phys. Rev. Lett. 89 (19) (2002) 196401.
[79] Y. Jiang, S. Pillai, M.A. Green, Re-evaluation of literature values of silver optical constants, Opt. Express 23 (3) (2015) 2133–2144.
[80] C.-Y. Tan, Y.-X. Huang, Dependence of refractive index on concentration and temperature in electrolyte solution, polar solution, nonpolar solution, and protein solution, J. Chem. Eng. Data 60 (10) (2015) 2827–2833.